

Supplementary Information

**Buseong Kim^{a,1}, Hojun Moon ^{a,1}, Byeong Sub Kwak^{b,1}, Dowon Jang^a, Harim Jeong^a,
Younghwon Kim^a, Geunhyeong Kim^a, Youngsoo Kim^{a,*}, Younghwan Im^{c,*}, Misook
Kang^{a,*}**

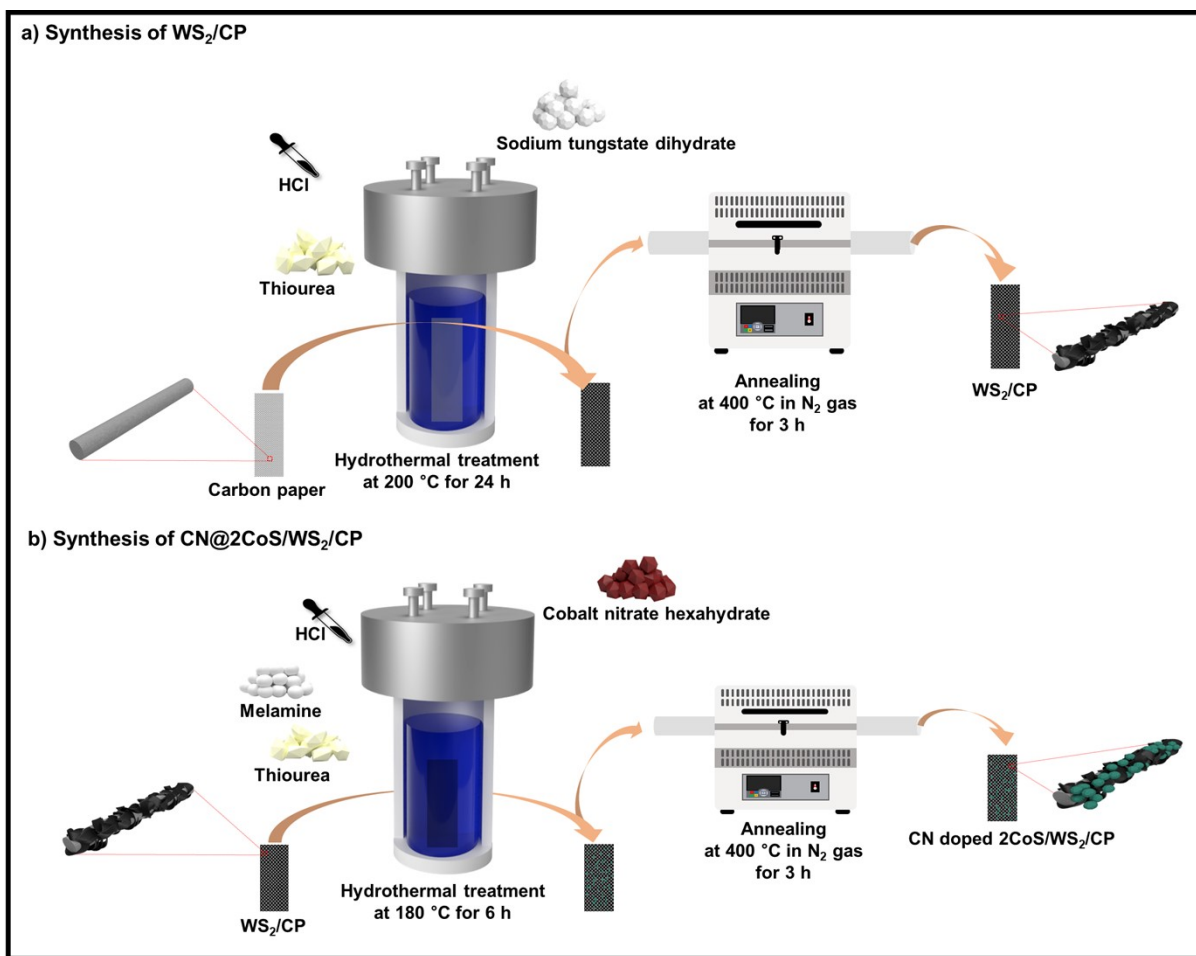
*^aDepartment of Chemistry, College of Natural Sciences, Yeungnam University, Gyeongsan,
Gyeongbuk 38541, Republic of Korea*

*^bKorea Electric Power Research Institute, Korea Electric Power Corporation, 105 Munji-ro,
Yuseong-gu, Daejeon 34056, Republic of Korea*

*^cKorea Research Institute of Chemical Technology (KRICT), 141 Gajeong-Ro, Yuseong-Gu,
Daejeon, 34114, Republic of Korea*

¹These authors are equally contributed to this study

*Corresponding authors: kimys6553@yu.ac.kr (Y. Kim), y.im@krikt.re.k (Y. Im),
miskang@ynu.ac.kr (M. Kang)



Scheme S1. Schematic illustration of the synthesis procedures for WS_2/CP and $\text{CN}@2\text{CoS}/\text{WS}_2/\text{CP}$.

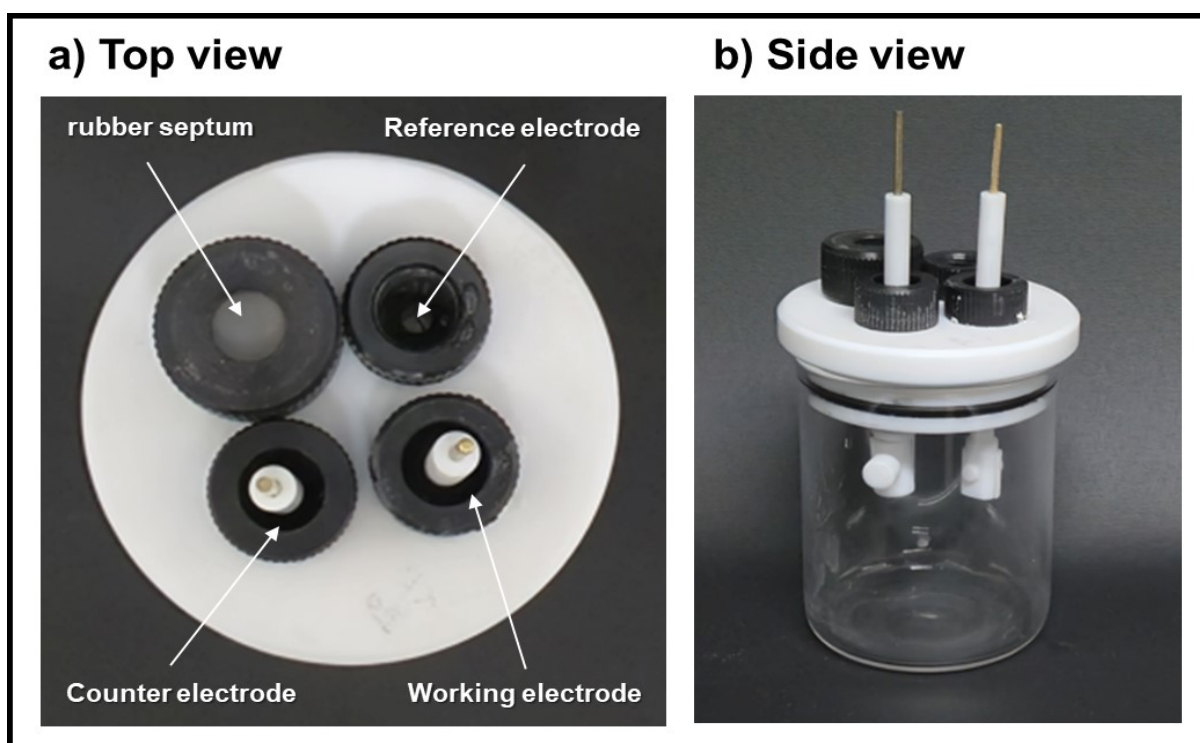


Fig. S1. Photographs of the H₂ gas collection setup used for FE measurements, showing the (a) top view and (b) side view of the sealed three-electrode cell with gas sampling ports. The evolved H₂ gas was collected and quantified using a gas-tight syringe connected through a septum under ambient laboratory conditions (25 ± 1 °C, 1 atm).

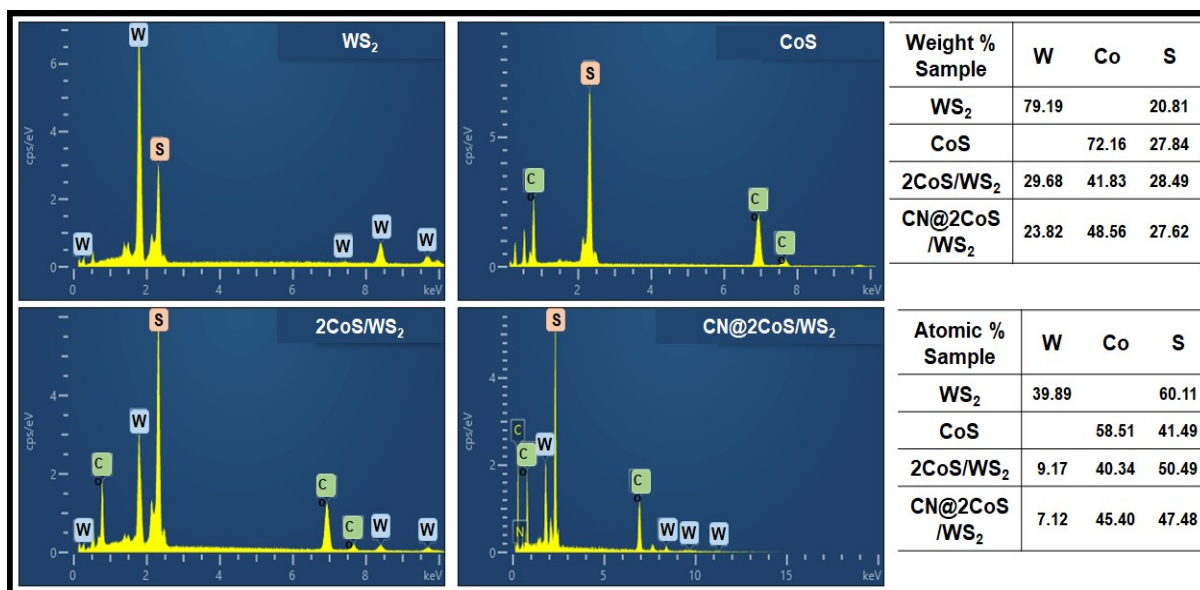


Fig. S2. EDS spectra and corresponding elemental compositions (weight % and atomic %) of WS_2 , CoS , $2CoS/WS_2$, and $CN@2CoS/WS_2$ samples.

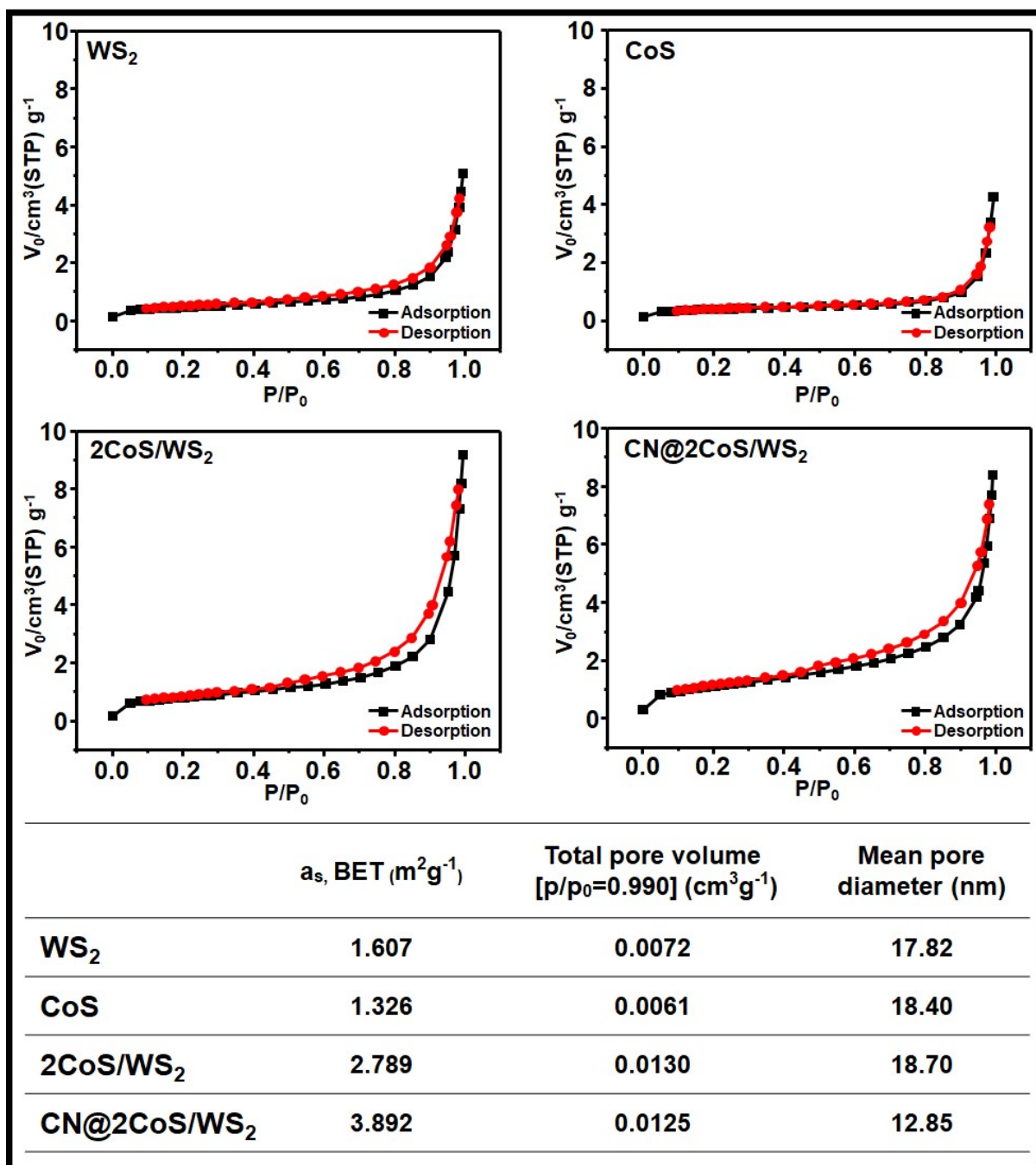


Fig. S3. N₂ adsorption–desorption isotherms and corresponding BET surface area, total pore volume, and mean pore diameter of WS₂, CoS, 2CoS/WS₂, and CN@2CoS/WS₂ samples.

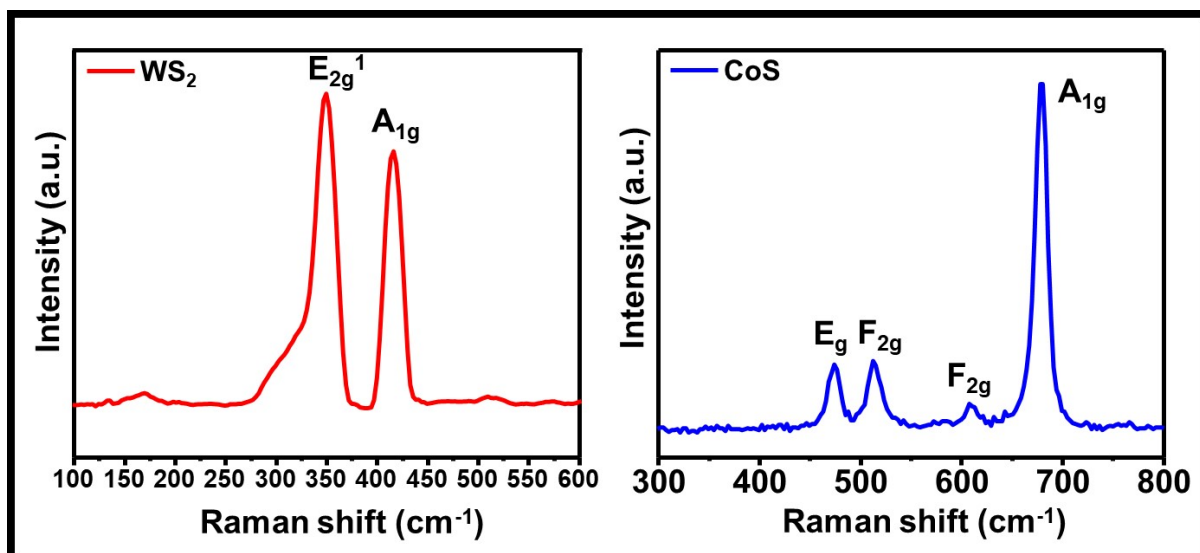


Fig. S4. Raman spectra of pristine WS₂ (left) and CoS (right).

WS₂ exhibits two characteristic vibrational modes, the in-plane E_{2g} (~356 cm⁻¹) and the out-of-plane A_{1g} (~418 cm⁻¹), consistent with hexagonal 2H-WS₂. CoS displays multiple features including the E_g, F_{2g}, and A_{1g} modes, with the dominant A_{1g} peak located near 680–700 cm⁻¹, confirming the crystalline structure of hexagonal CoS. These distinct Raman signatures validate the phase purity of each component prior to heterostructure assembly.

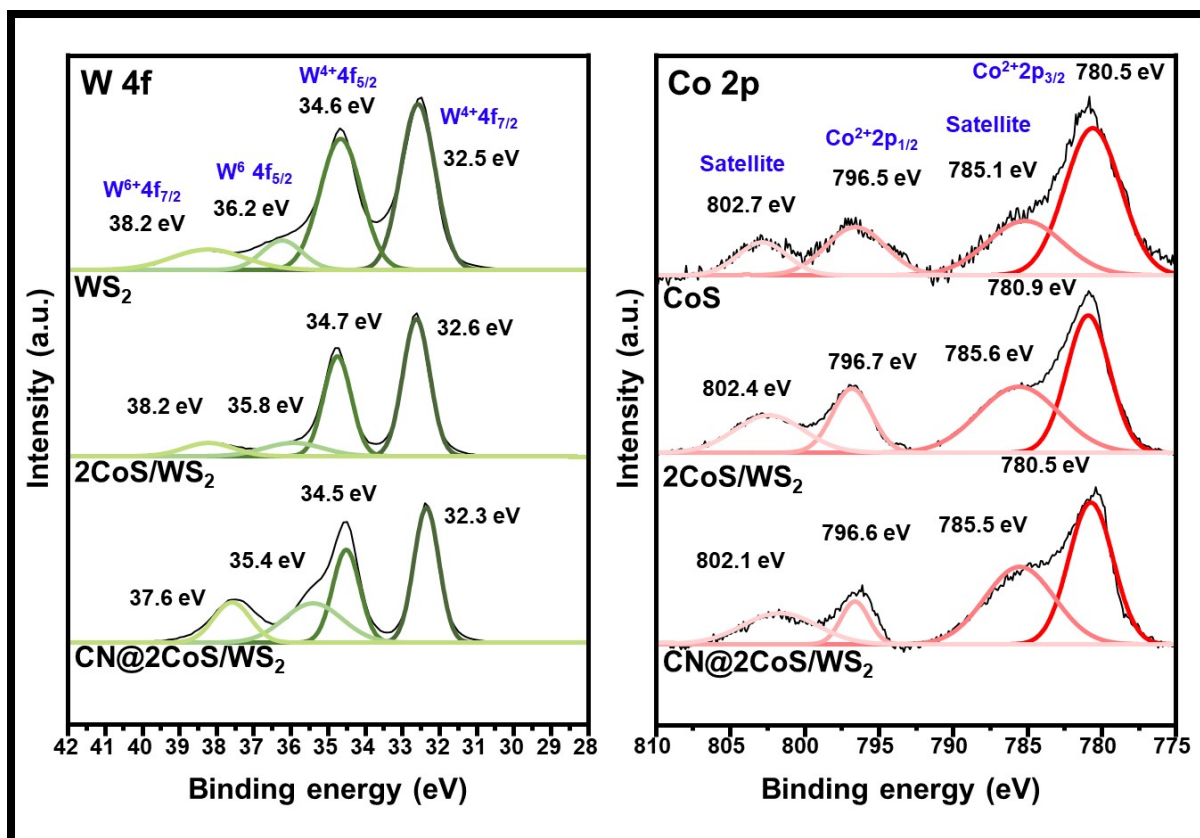


Fig. S5. High-resolution XPS spectra of (left) W 4f and (right) Co 2p regions for pristine WS₂, 2CoS/WS₂, and CN@2CoS/WS₂ electrodes.

For WS₂, the dominant W⁴⁺ 4f_{7/2} and W⁴⁺ 4f_{5/2} peaks appear at ~32.6 and ~34.7 eV, respectively, with a minor W⁶⁺ contribution at higher binding energies. After CoS incorporation, the W 4f peaks shift slightly to lower binding energies, indicative of interfacial electronic coupling. In the Co 2p spectra, Co²⁺ 2p_{3/2} is centered at ~780.9 eV with pronounced satellite peaks; upon hybridization with WS₂ and subsequent CN coating, both the Co 2p_{3/2} peak and satellite features shift to lower binding energy (~780.5 eV), accompanied by suppressed satellite intensity, signifying electron enrichment of Co centers and stabilization by the CN shell. These results confirm interfacial charge redistribution across the Co–W–S junction and the protective role of the amorphous CN layer.

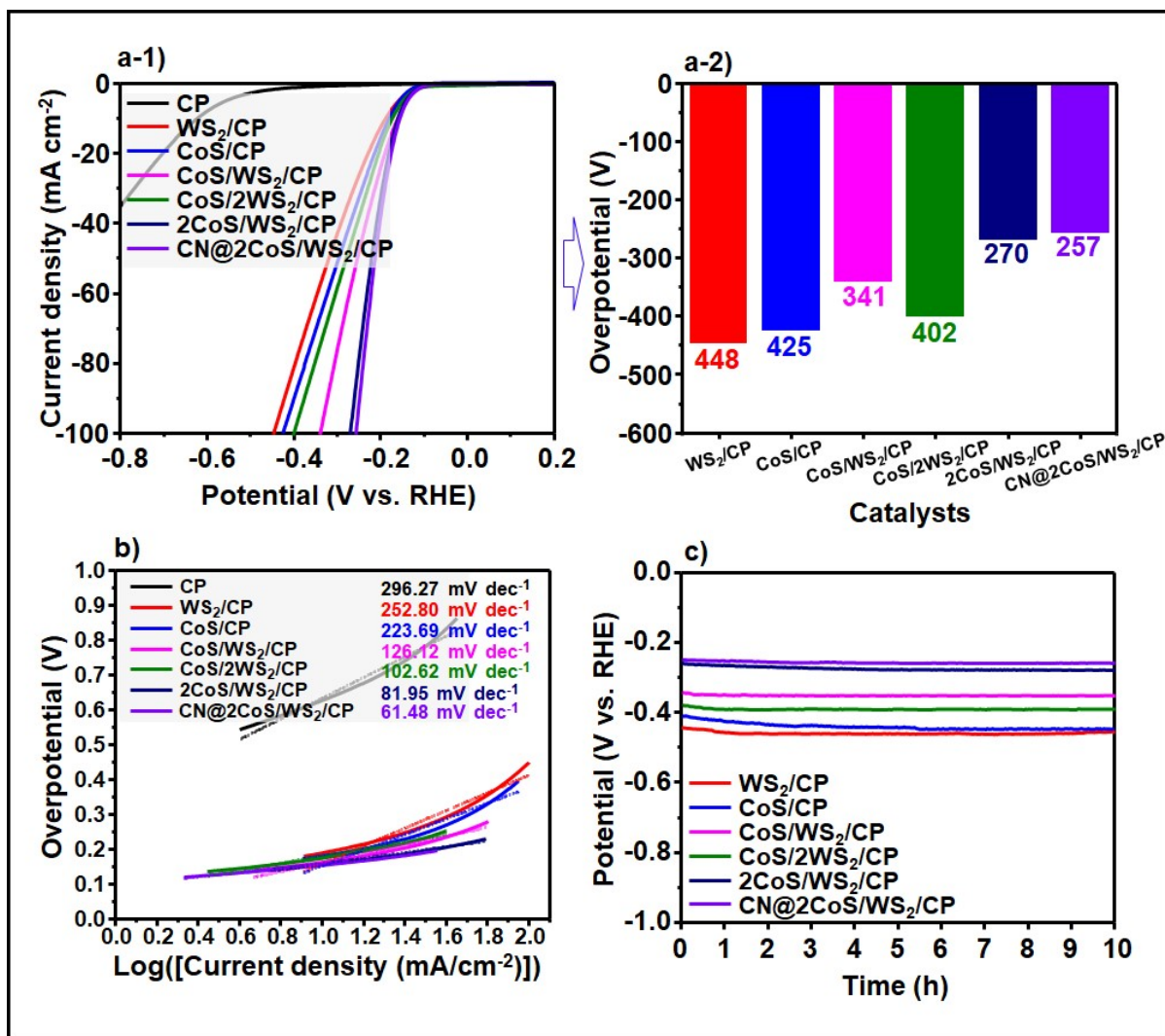


Fig. S6. Non-iR-corrected HER data corresponding to Fig. 4. (a-1) Non-iR-corrected polarization curves for WS₂/CP, CoS/CP, CoS/WS₂/CP, 2CoS/WS₂/CP, and CN@2CoS/WS₂/CP (corresponds to Fig. 4a-1). (a-2) Overpotentials at 10 mA cm⁻² extracted from the same non-iR-corrected LSV curves (corresponds to Fig. 4a-2). (b) Non-iR-corrected Tafel slopes derived from the polarization curves (corresponds to Fig. 4b). (c) Non-iR-corrected chronopotentiometry at 10 mA cm⁻² for 10 h (corresponds to Fig. 4e).

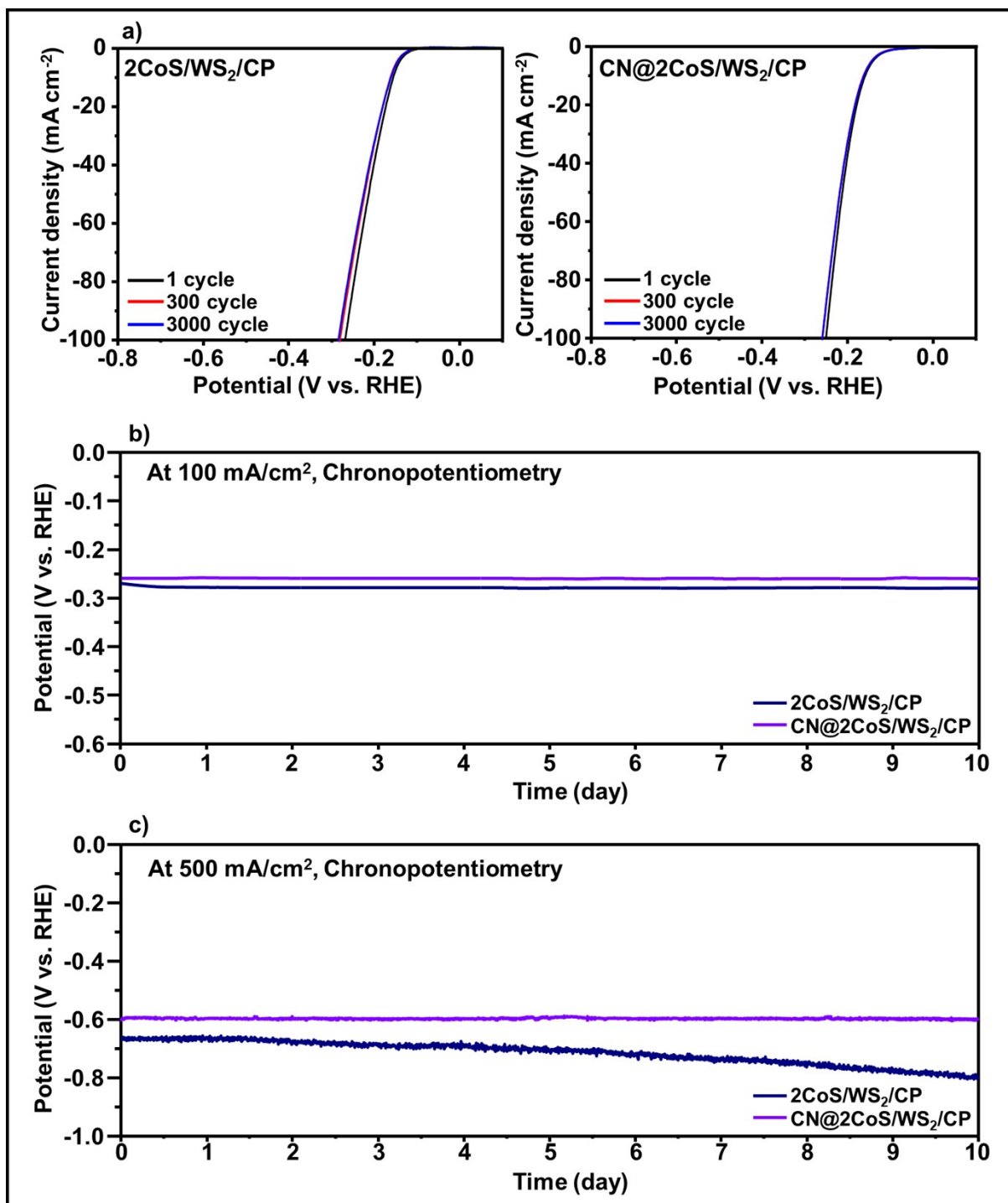


Fig. S7. Non-*iR*-corrected stability results corresponding to Fig. 5c, Fig. 6a, and Fig. 6b. (a) Non-*iR*-corrected LSV curves of 2CoS/WS₂/CP and CN@2CoS/WS₂/CP after 1, 300, and 3000 cycles, corresponding to Fig. 5c. (b) Non-*iR*-corrected chronopotentiometry at 100 mA cm⁻², corresponding to Fig. 6a. (c) Non-*iR*-corrected chronopotentiometry at 500 mA cm⁻², corresponding to Fig. 6b.

Table S1. Electrochemical impedance parameters (R_s and R_{ct}) of WS_2/CP , CoS/CP , $CoS/WS_2/CP$, $CoS_2/WS_2/CP$, $2CoS/WS_2/CP$, and $CN@2CoS/WS_2/CP$ electrodes obtained from Nyquist fitting.

Sample	R_s (Ω)	R_{ct} (Ω)
	(Solution Resistance)	(Charge Transfer Resistance)
WS_2/CP	1.05	25.8
CoS/CP	1.24	20.1
$CoS/WS_2/CP$	1.15	7.9
$CoS/2WS_2/CP$	1.20	15.2
$2CoS/WS_2/CP$	1.19	5.8
$CN@2CoS/WS_2/CP$	1.08	4.3

R_s corresponds to the uncompensated solution resistance, and R_{ct} represents the charge-transfer resistance associated with HER kinetics in 0.5 M H_2SO_4 .

< TOF calculation for CN@2CoS/WS₂/CP (corresponding to Fig. 5a)>

The turnover frequency (TOF) for hydrogen evolution was calculated using:

$$TOF = \frac{j_{geo} \cdot A}{2F \cdot n_{active\ site}}$$

where

- j is the geometric current density ($A\ cm^{-2}$),
- A is the electrode area ($1\ cm^2$),
- F is the Faraday constant ($96,485\ C\ mol^{-1}$),
- the factor of 2 corresponds to the two electrons required to form one H_2 molecule.

<Determination of active-site number (n_{sites})>

The number of catalytically active Co sites ($n_{active\ sites}$) was estimated from the integrated charge of the Co^{2+}/Co^{3+} redox peak:

$$n_{sites} = \frac{Q_{Co}}{F}$$

where Q_{Co} is the integrated charge of the Co^{2+}/Co^{3+} redox peak after subtracting the capacitive background. This approach is widely used because each Co redox event corresponds to one accessible active site.

< Representative values for CN@2CoS/WS₂/CP>

- Integrated Co redox charge: $\approx 1.7\ mC$
- Active sites: $n_{sites} \approx 1.76 \times 10^{-8}\ mol$
- At 0.25 V vs RHE ($j \approx 0.6\ A\ cm^{-2}$):

$$TOF = 0.168\ s^{-1}$$

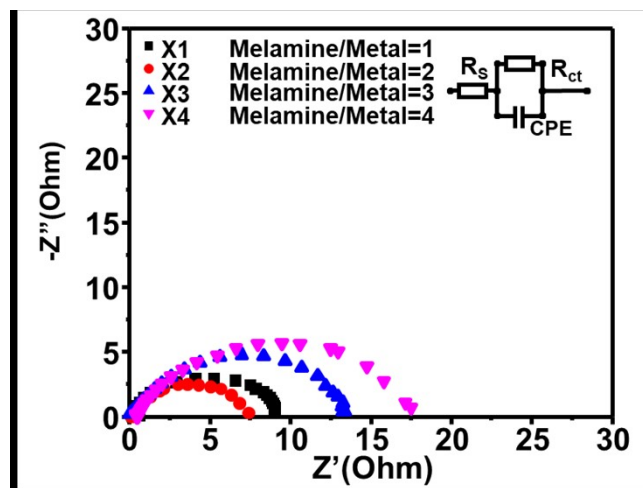


Fig. S8. Electrochemical impedance spectroscopy (EIS) Nyquist plots of CN@CoS/WS₂/CP electrodes synthesized with different melamine-to-metal precursor ratios (X1: 1, X2: 2, X3: 3, X4: 4).

The optimized sample (X2) exhibits the smallest semicircle radius, corresponding to the lowest charge-transfer resistance (R_{ct}), confirming that an appropriate CN coating thickness enhances electronic conductivity and interfacial charge transport. Excessive melamine loading (X3, X4) leads to increased R_{ct} due to thicker insulating CN layers, while insufficient melamine (X1) provides less effective coverage. These results highlight the critical role of controlled CN deposition in balancing conductivity and protection of the heterostructure.

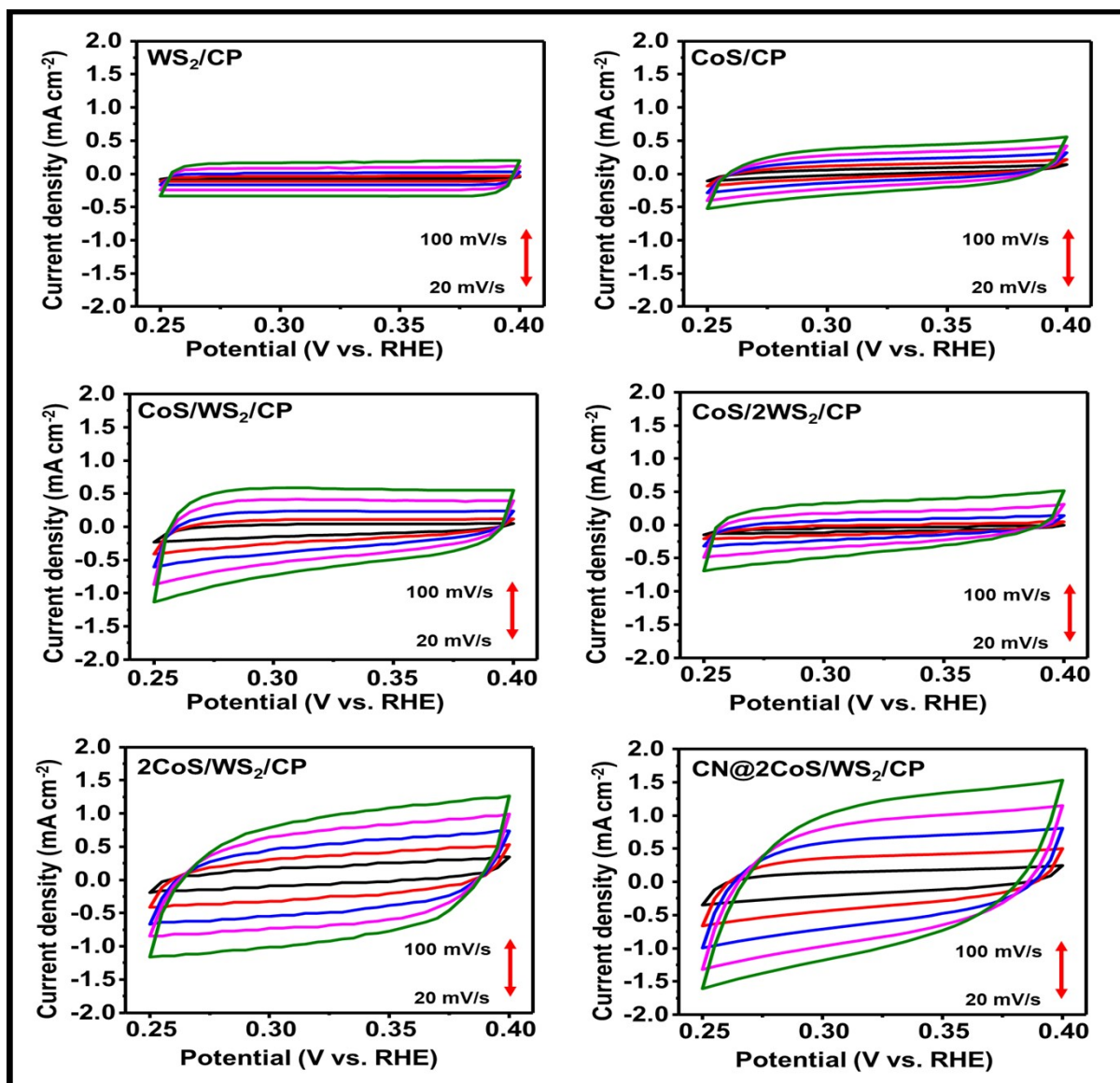


Fig. S9. Cyclic voltammograms (CVs) of WS₂/CP, CoS/CP, CoS/WS₂/CP, CoS/2WS₂/CP, 2CoS/WS₂/CP, and CN@2CoS/WS₂/CP electrodes recorded at different scan rates (20–100 mV s⁻¹) within a non-faradaic potential window.

The slope of capacitive current versus scan rate was used to estimate the double-layer capacitance (C_{dl}), which correlates with the electrochemically active surface area (ECSA). Among all samples, CN@2CoS/WS₂/CP displays the highest capacitive currents and largest C_{dl} values, confirming that CN modification significantly enhances accessible active sites and interfacial charge storage capability.

Table S2. HER performance comparison of CN@2CoS/WS₂/CP with representative WS₂- and CoS-based catalysts from the literature.

Catalyst	Electrolyte	Substrate	η_{10} , η_{100} (mV)	Ref.
CN@2CoS/WS ₂ /CP	0.5 M H ₂ SO ₄	Carbon Paper	η_{10} = 154 η_{100} = 176	This work
W ₁₈ O ₄₉ @WS ₂ NRs	0.5 M H ₂ SO ₄	Glassy Carbon	η_{100} = 310	[33]
1T-WS ₂ nanohelix	0.5 M H ₂ SO ₄	Glassy Carbon	η_{10} = 170	[34]
WS ₂ nanosheet	0.5 M H ₂ SO ₄	Nickel Foam	η_{100} = 280	[35]
WS ₂ nanorattle	0.5 M H ₂ SO ₄	Glassy Carbon	η_{10} = 193	[36]
WS ₂ -600	0.5 M H ₂ SO ₄	W	η_{10} = 155	[37]
Fe ₇ S ₈ /CoS	1 M KOH	Nickel Foam	η_{10} = 216	[38]
Co/CoS ₂ @NC-2	0.5 M H ₂ SO ₄	Glassy Carbon	η_{10} = 187	[39]
CoS _{1.097} -160	0.5 M H ₂ SO ₄	Glassy Carbon	η_{10} = 163	[40]
rGO-CoS/CoS ₂ @P5	0.5 M H ₂ SO ₄	Glassy Carbon	η_{10} = 169	[41]
CoS/CC	0.5 M H ₂ SO ₄	Carbon Cloth	η_{10} = 268	[42]

Unless noted, tests were conducted in 0.5 M H₂SO₄. Our electrode combines low overpotentials (η_{10} = 154 mV; η_{100} = 176 mV) with binder-free integration on carbon paper and long-term acid stability at high current densities (this work).

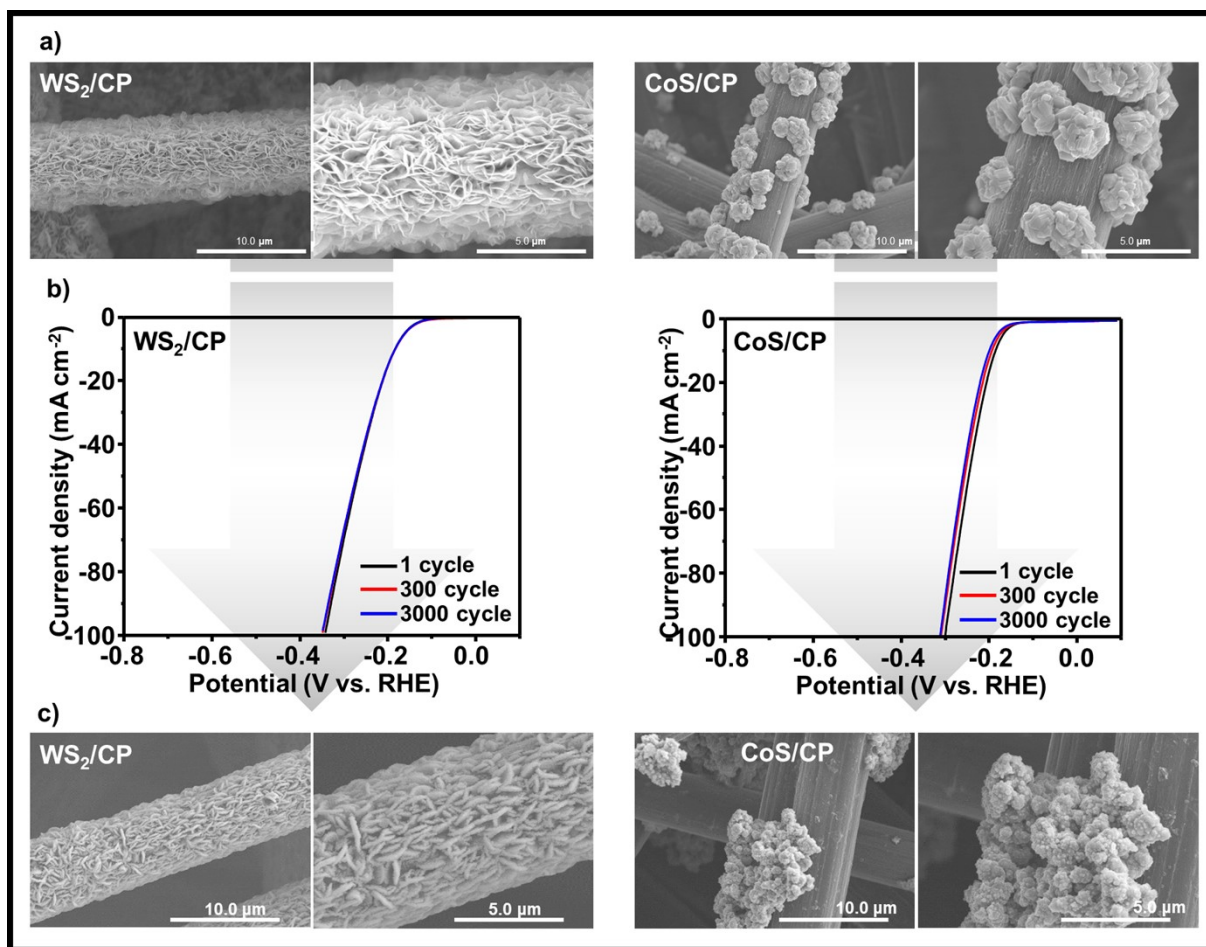


Fig. S10. Durability evaluation of pristine WS₂/CP and CoS/CP electrodes. (a) SEM images of freshly prepared electrodes, showing nanosheet arrays for WS₂ and aggregated nanoparticle clusters for CoS. (b) Polarization curves recorded before and after accelerated durability tests (1, 300, and 3000 cycles) at 100 mV s⁻¹ in 0.5 M H₂SO₄, indicating negligible performance loss for both electrodes. (c) SEM images collected after 3000 cycles confirm that the overall morphologies of WS₂ nanosheets and CoS nanoparticles are preserved, demonstrating intrinsic structural robustness of the individual components under acidic HER conditions.

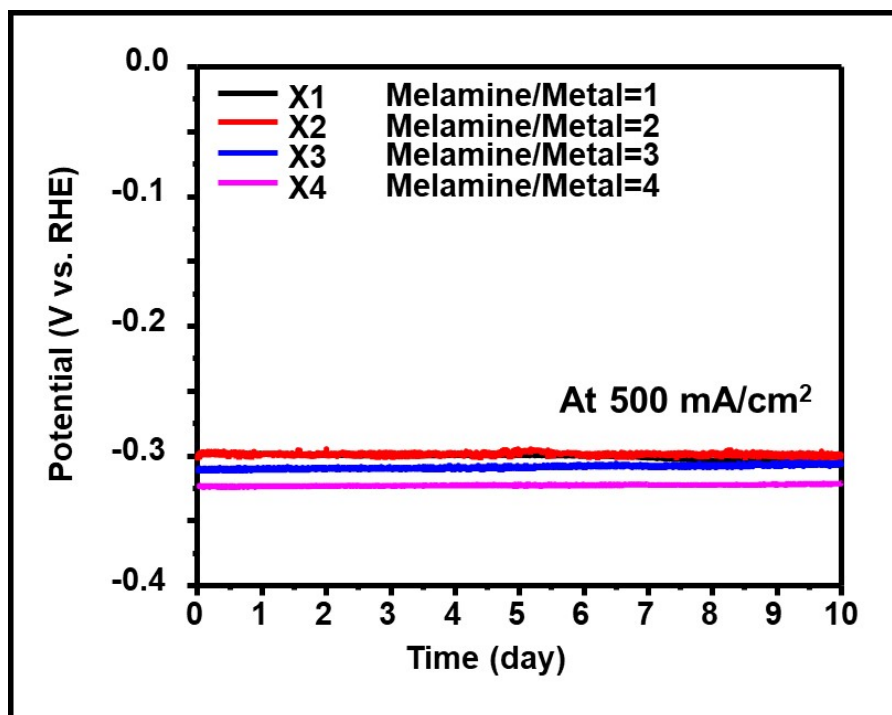
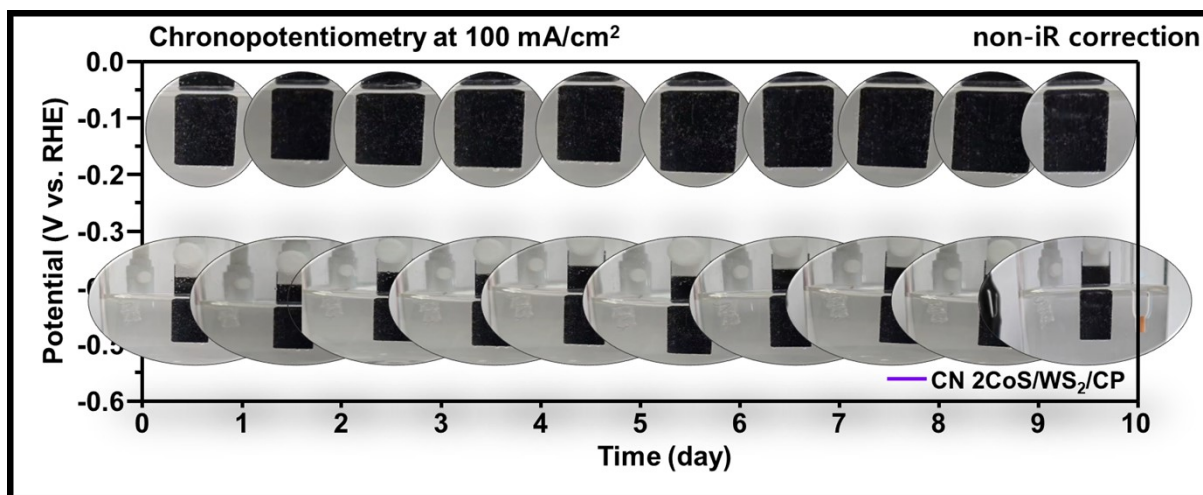


Fig. S11. Chronopotentiometric stability tests of CN@CoS/WS₂/CP electrodes synthesized with varying melamine-to-metal ratios (X1: 1, X2: 2, X3: 3, X4: 4), conducted at a constant current density of 500 mA cm⁻² in 0.5 M H₂SO₄ for 10 days.

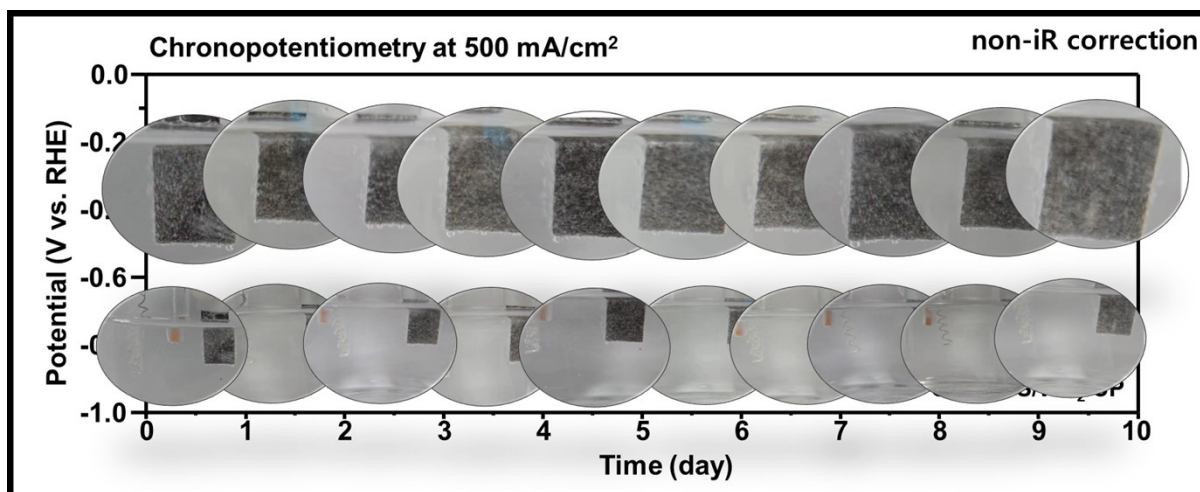
The optimized electrode (X2) maintains the most stable potential (≈ -0.60 V vs. RHE) over the entire duration, highlighting the critical role of controlled CN coating in enhancing durability. Electrodes with lower CN content (X1) suffer from gradual degradation due to insufficient protection, whereas those with excessive CN (X3, X4) show slightly higher overpotentials arising from increased resistive layers.



Movie S1. Real-time chronopotentiometric stability test of CN@2CoS/WS₂/CP electrode at 100 mA cm⁻² in 0.5 M H₂SO₄ for 10 days.

The potential remains nearly constant throughout the extended operation, and continuous hydrogen bubble evolution can be clearly observed, evidencing excellent catalytic durability and Faradaic efficiency under acidic conditions.

→ Attached separately as a video 1



Movie S2. Real-time chronopotentiometric stability test of CN@2CoS/WS₂/CP electrode at an industrially relevant current density of 500 mA cm⁻² in 0.5 M H₂SO₄ over 10 days.

The electrode maintains a nearly constant potential with vigorous hydrogen bubble evolution, confirming both outstanding durability and efficient proton-to-hydrogen conversion even under harsh acidic and high-current conditions.

→ Attached separately as a video 2

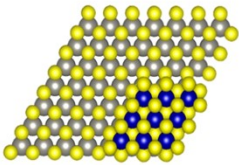
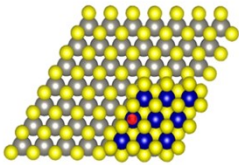
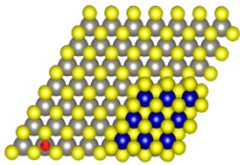
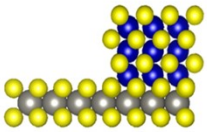
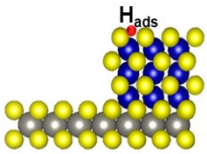
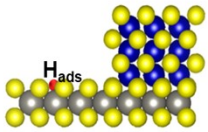
Sample	2CoS/WS ₂	H→W-2CoS/WS ₂	H→Co-2CoS/WS ₂
E _{DFT}	-414.33 eV	-414.51 eV	-414.40 eV
Top view			
Side view			

Fig. S12. Optimized DFT models of the 2CoS/WS₂ interface before and after hydrogen adsorption.

Top and side views are shown for (left) pristine 2CoS/WS₂, (middle) H adsorbed on a W site (H→W-2CoS/WS₂), and (right) H adsorbed on a Co site (H→Co-2CoS/WS₂). The calculated total energies (E_{DFT}) are -414.33 eV, -414.51 eV, and -414.40 eV, respectively, indicating that H adsorption at both W and Co interfacial sites is thermodynamically favorable. These results corroborate the experimentally observed synergistic catalytic behavior of Co-W-S junctions, where interfacial Co and W centers cooperatively optimize hydrogen binding energies for efficient HER.